Design of Ni/NiO–TiO2/rGO nanocomposites on carbon cloth conductors via PECVD for electrocatalytic water splitting

Heba H. El-Maghrabi, Amr A. Nada, Stéphanie Roualdes, Maged F. Bekheet

Design of Ni/NiO-TiO_2/rGO nanocomposites on carbon cloth conductors via PECVD for electrocatalytic water splitting

Heba H. El-Maghrabi[a,b], Amr A. Nada[b,c,*], Stéphanie Roualdes[b] and Maged F. Bekheet[d]

[a] Dept. of Refining, Egyptian Petroleum Research Institute, Cairo, Nasr city P.B. 11727, Egypt

[b] Institut Européen des Membranes, IEM–UMR 5635, ENSCM, CNRS, Univ Montpellier, Montpellier, France

[c] Dept. of Analysis and Evaluation, Egyptian Petroleum Research Institute, Cairo, Nasr city P.B. 11727, Egypt

[d] Fachgebiet Keramische Werkstoffe/Chair of Advanced Ceramic Materials, Institut für Werkstoffwissenschaften und -technologien, Technische Universität Berlin, Hardenbergstraße 40, 10623 Berlin, Germany

Abstract

The facile synthesis and design of noble metal-free efficient catalysts to accelerate the sluggish kinetics of the hydrogen evolution reaction (HER) and oxygen evolution reaction (OER) is still a big challenge for electrolytic water splitting. In that context, the preparation of efficient catalysts with superior catalytic activity from cheap raw materials on a large scale is crucial. Briefly, Ni/NiOTiO_2/rGO is designed using the environmental-friendly and easily up-scalable PECVD technique. This trinary composite presents significance in regulating the crystalline structure, composition and electronic properties towards superior HER and OER activity in acidic solution as bifunctional electrocatalysts for efficient water splitting. Together with the promising long-term stability and durability, Ni/NiOTiO_2/rGO displays excellent HER with η_{10} of 130 mv vs RHE and a Tafel slope of 40 mV/dec.

Key Words: Water Splitting, HER, OER, Ni/NiO, TiO_2, reduced graphene oxide, PECVD.

Introduction

Hydrogen will be an alternative clean and inexhaustible source of energy in the near future as the fossil-fuel age wanes. Hydrogen could be produced by electrolysis or water splitting using photo- or electrocatalysts [1-6]. The control of the hydrogen evolution reaction (HER) and oxygen evolution reaction (OER) during the water-

splitting process is challenging and might require an expensive electrocatalyst of noble metals [7-10]. However, the use of these expansive electrocatalysts increases the cost of hydrogen production. Thus, several researchers have recently used low-cost and durable earth-abundant metal oxide of Fe, Ti, Co, Zn, and Ni as electrocatalysts [11-20]. Numerous synthetic techniques, including chemical vapor deposition [21-24], hydrothermal [25, 26], and electrodeposition [27], have been developed to fabricate active nano-sized metal oxides with enhanced performance. However, large-scale manufacturing of high-performance oxide electrocatalysts remains very difficult [28-30]. Except for beneficent activity maintaining, the stability of the catalysts on the substrates has been admitted as one more challenge to enable the stable function of the electrodes [31, 32]. Although several additives and binders have been applied to enforce the adhesion between electrocatalysts and substrates, the electrodes still suffer from the instability, materials agglomeration, and peeling-off, which limits the long-term activities of the electrocatalysts. Moreover, the large-scale fabrication of low-cost and stable electrocatalyst electrodes with high-performance presents another crucial challenge [33-38]. The arrangement of different hybrids materials with metal oxides has reinforced their dispersion and electrical conductivity on conductive supports with a large number of active sites on porous surfaces [39]. In particular, the graphene-based carbon materials, including carbon nanotubes [39-43], reduced graphene oxide [44-48], graphene shells [49], and carbon fibers have been provided an effective conducting network for electron transfer, massive pore structures for ion transport, and large surface areas for the electrochemical reactions.

Recently, several works have reported that the combination of NiO (p-type) and TiO_2 (n-type) in one material could produce effective catalysts due to the formation of *p-n* heterostructure [50-52]. For instance, Chen *et al.* have explained the excellent catalytic activity of NiO/TiO_2 for the degradation of methylene blue by the formation of *p-n* junction in addition to the cocatalyst effect of TiO_2 and NiO [50]. The *p-n* junction formed in the NiO/TiO_2 photocatalyst could facilitate the electron-hole separation due to the generation of an internal electric field in the material [50]. Moreover, this internal electrical field could enhance the flow of current under the forward bias, resulting in a minimum resistance [50]. Thus, the catalytic performance of materials containing NiO/TiO_2 heterostructures for water

electrolysis is expected to be enhanced due to low resistance and the high probability of electron-hole separation in the *p-n* junction.

Moreover, the addition of metallic Ni to this heterostructure could enhancement the charge separation for water splitting, thus enriched the hydrogen production activity. For example, Yu *et al.* elaborated Ni-$Ni(OH)_2$-TiO_2 nanocomposite for H_2 production [51]. Metallic Ni could play an essential role in enhancing HER and OER by increasing the conductivity, current flow, and stability of the prepared electrode [53, 54]. Thus, there is a synergism effect of *p-n* junction and metallic Ni to reduce the resistivity and enriched the conductivity in the Ni/NiO/TiO_2 materials. It has been reported that the rGO based nanomaterials show ascendant electrical properties [55, 56], which could facilitate the electron transfer in any composites containing them. Thus, similar to Ni and NiO, the addition of rGO to TiO_2-based catalysts, such as Fe_3O_4/rGO/TiO_2 and $NiTiO_3$-rGO, could improve their activities for dye degradation and water splitting due to the enhancement of electron transfer [48, 57-60]. Considering both Ni and rGO are effective in improving the performance of NiO/TiO_2 (*p-n* junction). Herein, the combination of rGO, Ni, NiO, and TiO_2 in one heterostructure can be a unique method to improve the catalytic performance for HER and OER.

Plasma enhanced chemical vapor deposition (PECVD), which is well-known in the microelectronic domain as an environmental-friendly and easily up-scalable deposition technique, has been widely applied to produce diverse nanostructured thin films on various solid surfaces with advantages of being one-step, mask-less, non-contact, highly-efficient, easily adapted and facially controlled [47, 61]. Herein, we report a novel one-pot fabrication of hierarchical nanostructured hybrid nanocomposites directly grown on carbon cloth substrate by fast PECVD. A unique structure of Ni/NiOTiO_2/rGO nanocomposite has been successfully *in situ* grown on the surface of carbon cloth size of 4cm×4cm within a short time and could be directly applied as high-performance bifunctional electrodes for electrocatalytic water splitting (both HER and OER). To our knowledge, there are no reports on the catalytic H_2 production over Ni/NiOTiO_2/rGO on CC by PECVD. The main objective of this study is to demonstrate that the large-scale hierarchical nanostructured composites have high catalytic activities as well as long-term stability for electrocatalytic overall water splitting.

Experimental

Materials:

Pure sulfuric acid H_2SO_4 (100%) was obtained from Merck. Titanium (IV) tetraisopropoxide (TTIP) (99.999%), nickel nitrate (99.99%), Graphite (CAS number 7782-42-5), sodium nitrate (99%), potassium permanganate (99%) and hydrogen peroxide (30%) were purchased from Sigma Aldrich. All the chemicals were used without any further purification. A porous conductive carbon cloth (E-Tek, country USA) was used as a substrate. The Argon gas (99.999%) and the oxygen gas (99.5%) were purchased from Linde company.

Preparation methods:

Graphene oxide (GO) was synthesized by the oxidation of graphite using the modified Hummer method, as described in the literature [62-64].

The fabrication of the nanocomposites on carbon cloth substrate was performed using PECVD process based on the procedure introduced by Nada et al. [47, 65] as follows. A carbon cloth (CC) piece 4x4 cm was positioned on a heated (at 350°C with a Eurotherm heating device) ground electrode (diameter 10 cm) of a vacuumed (1 Pa limit pressure commanded by an Alcatel pumping system and controlled by Tylan General ACX2211 Rev A ACX adaptor) PECVD capacitively-coupled reactor. For the preparation of G, N, and NG samples, the surface of the carbon cloth was preliminarily saturated with dispersing GO, nickel salt, and a mixture of GO and nickel salt in ethanol, respectively. For the preparation of the samples containing TiO_2, namely T, GT and NGT (the descriptions of all samples are illustrated in Table S1), the Ti-based precursor was carried into the deposition chamber by passing Ar through hot TTIP solution with $P_{Ar+TTIP}$ = 30 Pa; in the same time, O_2 gas as an oxidant was simultaneously introduced with P_{O2} = 10 Pa. In every case, the plasma discharge was generated with 50 W input power for 20 min inside the deposition chamber using an R.F. power generator (CESAR 136), coupled with a matching box (RF Navio, Advanced Energy) that was connected to an inner electrode (diameter 10 cm) on top of the chamber. The plasma discharge induced the reduction of GO into rGO and the plasma conversion of TTIP/O_2 into TiO_2.

Characterization methods:

The crystalline phase of the materials was analyzed by X-ray diffraction (XRD) using a PANAlytical Xpert-PRO diffractometer equipped with an Xcelerator detector using Ni-filtered Cu radiation (CuKα1 radiation wavelength 0.1540598 nm and CuKα2 radiation wavelength 0.1544426 nm). Raman spectra were conducted in Horiba XploRA (Horiba, Japan) using λ = 659 nm at a power of 10 W and a microscope objective lens of 100×. The morphology and chemical compositions of deposited samples were analyzed by scanning electron microscopy (SEM) in a Hitachi S4800 (Japan), and energy-dispersive X-ray spectroscopy (EDX) in a Zeiss EVO HD15 microscope (Zeiss, Germany) coupled to an Oxford X-MaxN EDX detector. The elemental composition on the surface of the samples were determined by X-ray photoelectron spectroscopy (XPS) on an Escalab 250 (Thermo Fisher Scientific, USA) using a monochromatic Al K Alpha (1486.6 eV) at 2kV and 1 μA.

The electrochemical tests were carried out by a solartron SI 1287 galvanostatic-potentiostat in a three-electrode configuration with a graphite counter electrode and Ag/AgCl (SI Analytics) reference electrode in a 0.5 M H_2SO_4 electrolyte solution (0.197 V vs. RHE at room temperature). During this measurement, the prepared samples were used as a working electrode in the form of a disc of 10 mm diameter with a constant surface area of 0.78 cm^2. A Pt wire (CH instruments, USA) was used on the cathode side as a standard material for comparison. The linear voltammetry (LV) curves were collected in the potential range of 0 V to -0.6 V for HER and 1.2 to 1.8 V for OER, both at a potential scan rate of 5 mV/s. The cyclic voltammograms (CV) were recorded in the potential range of 0.1 to 0.3 V at different scan rates of 10 to 100 mV/s. Potentials were referenced to a reversible hydrogen electrode (RHE) following the equation: $E_{RHE} = E_{Ag/AgCl} + 0.059 \times pH + 0.197$. The chronoamperometry test under an onset potential was performed during 60 h for the stability test of the deposited samples. Electrochemical Impedance Spectroscopy (EIS) was performed with a Solartron SI 1260 frequency analyzer from 10^5 to 0.1 Hz with 10 mV AC amplitude. For full water splitting measurement, the deposited samples were directly used as both anode and cathode in a standard two-electrode system. All electrochemical experiments were carried out at room temperature and at ambient pressure. Both ZPlot and ZView software were used to fit and record the experimental output data.

Results and Discussion

X-ray diffraction (XRD) was used to analyze the crystallinity and phase composition of the prepared samples, as illustrated in Fig.1 and Fig 1S. As shown in Fig 1S, only two broad reflections at 2θ = 26° and 43° corresponds to the planes (002) and (101), respectively, of the carbon cloth substrate (CC) [66], are observed on the XRD pattern of T, G, GT and CC samples. No other XRD reflections corresponding to any of the crystalline TiO_2 phases are observed, suggesting the amorphous nature of TiO_2 deposited on carbon cloth substrate. In contrast, a series of broad XRD reflections are observed on the XRD pattern of N, NT and NG samples, which can be assigned to the cubic structure of NiO (JCPDS card no. 047-1049). This result suggests the formation of nanocrystalline NiO phase through the plasma process without any further heat treatment, which agrees with previous works [67]. Rietveld refinement of XRD patterns reveals that the weight fraction of the nanocrystalline NiO phase (i.e., crystallite size is 2.5-3.5 nm) decreases from 35.3±0.4 wt% in N sample to 15.3±0.4 and 2.9±0.1 wt% in NT and NG samples, respectively. These results indicate that the presence of TiO_2 and rGO hinder the crystallization of NiO phase. Thus, no crystalline NiO is observed in NGT sample. In contrast, the lattice parameter *a* of the NiO phase does not change by the addition of TiO_2 and rGO, where, *a* = 4.1920(7), 4.1932(8) and 4.1931(7) Å for N, NT and NG sample, respectively, suggesting that no Ti or C are incorporated in the NiO lattice.

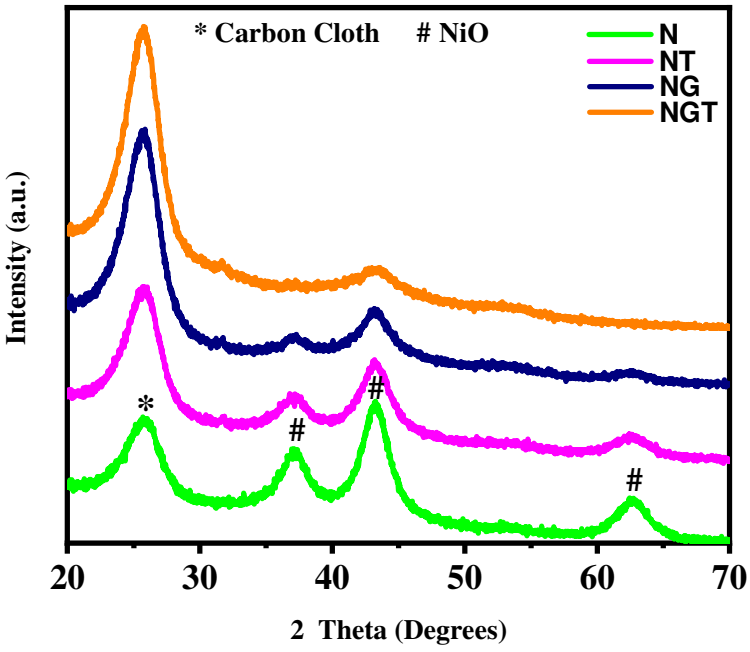

Fig. 1: XRD patterns of N, NT, NG and NGT samples on carbon cloth.

The chemical compositions and oxidation states of different elements on the surface of the obtained samples were studied using X-ray photoelectron spectroscopy analysis (XPS). The high-resolution XPS spectra of Ni 2p, Ti 2p, and O 1S orbitals are presented in Fig. 2 a-c. As shown in Fig. 2a, the Ni $2P_{3/2}$ spectrum of NG sample can be deconvoluted into a peak located at ~ 856 eV with a satellite at ~ 861.5 eV, which is in good agreement with previous reports for NiO [68]. The additional peak located at 853.4 in the spectrum of NTG sample can be attributed to metallic nickel Ni^0 [68, 69]. The ratio of Ni^0/Ni^{2+} in NGT sample calculated from XPS spectrum is about 0.15. These results are consistent with previous work showed the partial reduction of NiO to metallic Ni under non-oxidative plasma conditions in the presence of TiO_2 [52]. The Ti $2p_{3/2}$ spectra (Fig. 2b) can be fitted with a single peak located at 459.16 and 458.74 eV for TG and NGT samples, respectively, which is consistent with previous reports for TiO_2 [52]. The shift of Ti 2p peak to lower binding energy for NGT sample suggests the partial reduction of Ti^{4+} into Ti^{3+} and the formation of oxygen vacancies as charge compensation, which agrees with the partial reduction of Ni^{2+} in the sample. As shown in Fig. 2d, the O 1s spectra of the three samples can be deconvoluted into two peaks at ~529.6 and 532 eV corresponding to the oxygen lattice O_{latt} and hydroxides O_{hyd}, respectively [1]. The ratio of O_{hyd}/O_{latt} increases from 0.74 in TG sample to 1.03 in NGT sample, suggesting that the surface of NiO is more hydroxylated than that of TiO_2.

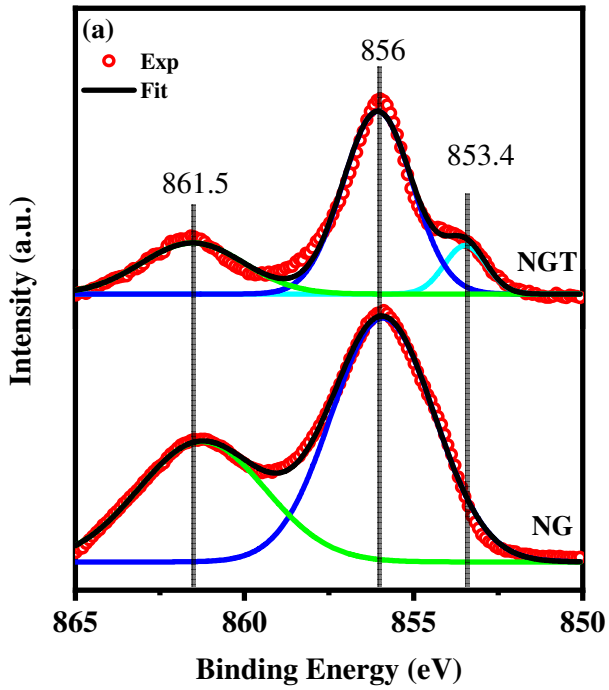
(a)
Exp
Fit
856
853.4
861.5
NGT
NG
Intensity (a.u.)
865
860
855
850
Binding Energy (eV)

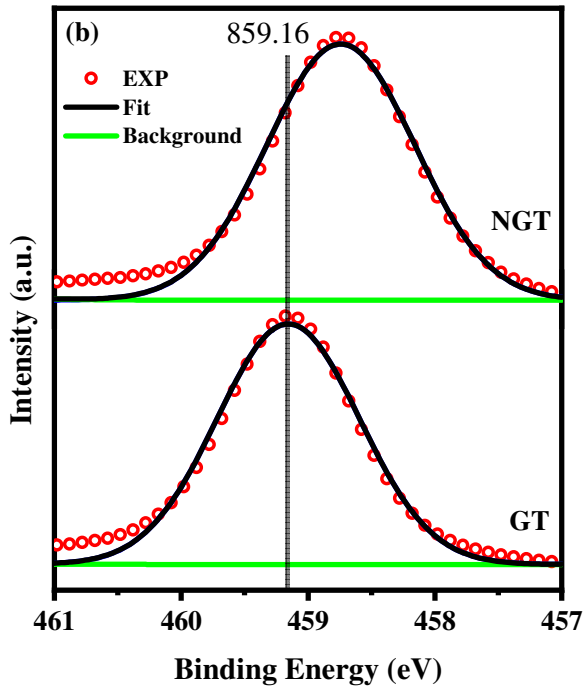
(b)
859.16
EXP
Fit
Background
NGT
GT
Intensity (a.u.)
461
460
459
458
457
Binding Energy (eV)

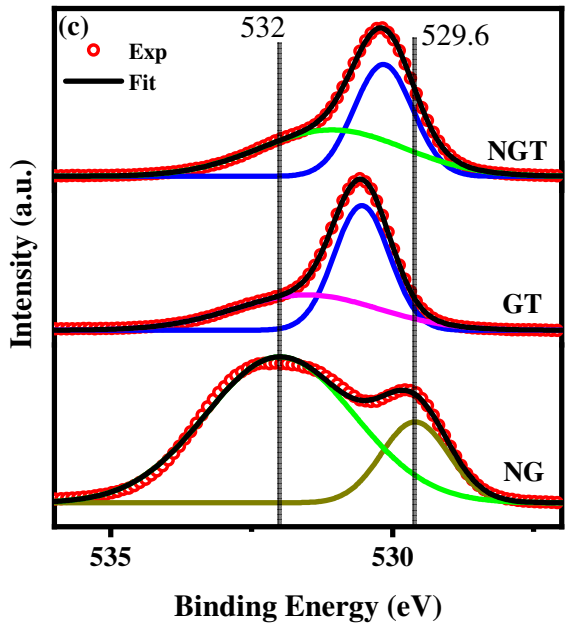

Fig. 2. High-resolution XPS spectra of Ni 2p (a), Ti 2p (b) and O 1s (c) for GT, NG and NGT samples.

The Raman spectra of T, G, GT, N, NT, NG, and NGT samples are shown in Fig.3a and b. The observed Raman modes can be assigned to the Raman spectra of the anatase crystal at 149.9 (E_g), 196.3 (E_g), 398 (B_{1g}), 514 (A_{1g}+ B_{1g}) and 622 (E_g) cm^{-1} [64, 70] in T and GT samples. However, the anatase phase is quenched in the presence of rGO and/or NiO, and an amorphous TiO_2 phase is observed in NT and NGT samples instead. This finding is in good agreement with XRD results. The formation of NiO phase in N, NG, NT, and NGT samples is confirmed by its Raman shift at about 500 cm^{-1} [69]. Moreover, the peaks at 1320 cm^{-1} (D band) and 1590 cm^{-1} (G band) can be assigned to rGO and CC [63, 71]. These two peaks are not observed in Raman spectra of NT and N samples prepared without rGO. These results suggest that the deposited NiO and TiO_2 layers are thick enough to prevent the detection of D and G bands of CC.

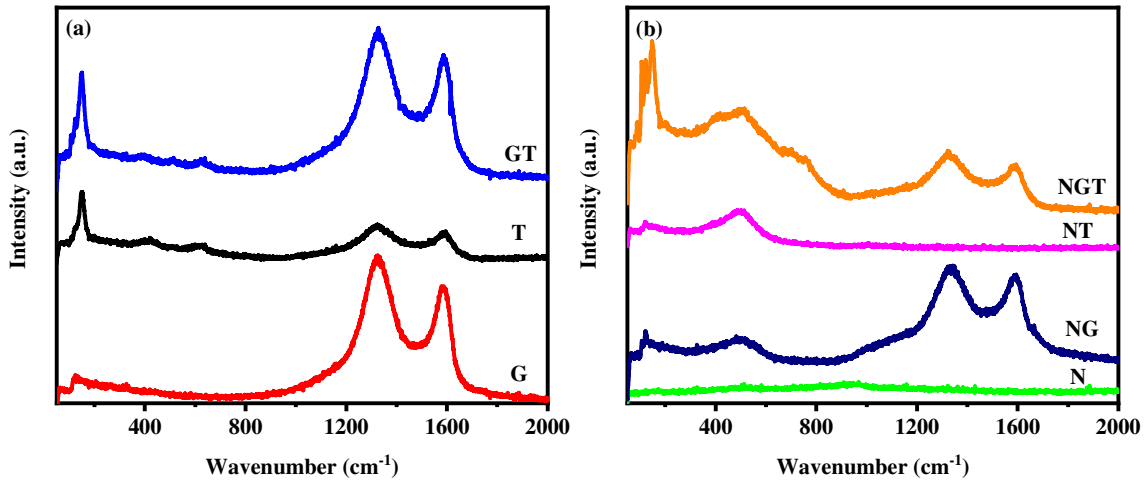

Fig. 3 (a) Raman spectra of G, T and GT samples. (b) Raman spectra of N, NG, NT and NGT samples.

The surface morphologies of the T, G, GT, N, NT, NG, and NGT samples were analyzed by SEM analysis (Fig. 4a-g). As shown in Fig 4a, the T sample consists of TiO_2 nanoparticles that have a crisscross-like overlapped pore interceded texture with an average diameter of 30 nm. The rGO forms a 3D porous network in the G samples (Fig. 4b), while the NiO is deposited as well-dispersed nanoflower like morphology in N sample (Fig. 4d). As shown in Fig 4e and g, the NiO and TiO_2 nanoparticles are randomly distributed on the surface of CC substrate in NT and NGT samples. At the same time, the rGO sheets tend to be deposited on the surface of these NiO and TiO_2 nanoparticles in GT, NG, and NGT samples. The elemental composition was confirmed by EDX analysis, as illustrated in Table S2. Furthermore, the weight fraction of NiO phase decreased in the presence of rGO, as presented in XRD. The results show that the main elements are C, Ti, O, and Ni. The elemental mapping analysis of NGT sample suggests the presence of C, O, Ni, and Ti elements, as demonstrated in Fig. S2. It is notable that the active sites of C and Ni have been established at the TiO_2 nanoparticles interface with very well dispersion in the top surface of the samples and manifesting that it is porous, and all the elements are homogeneously distributed. These results suggest an excellent charge transfer response toward electrochemical water splitting for the Ni/NiOTiO_2/rGO nanocomposite.

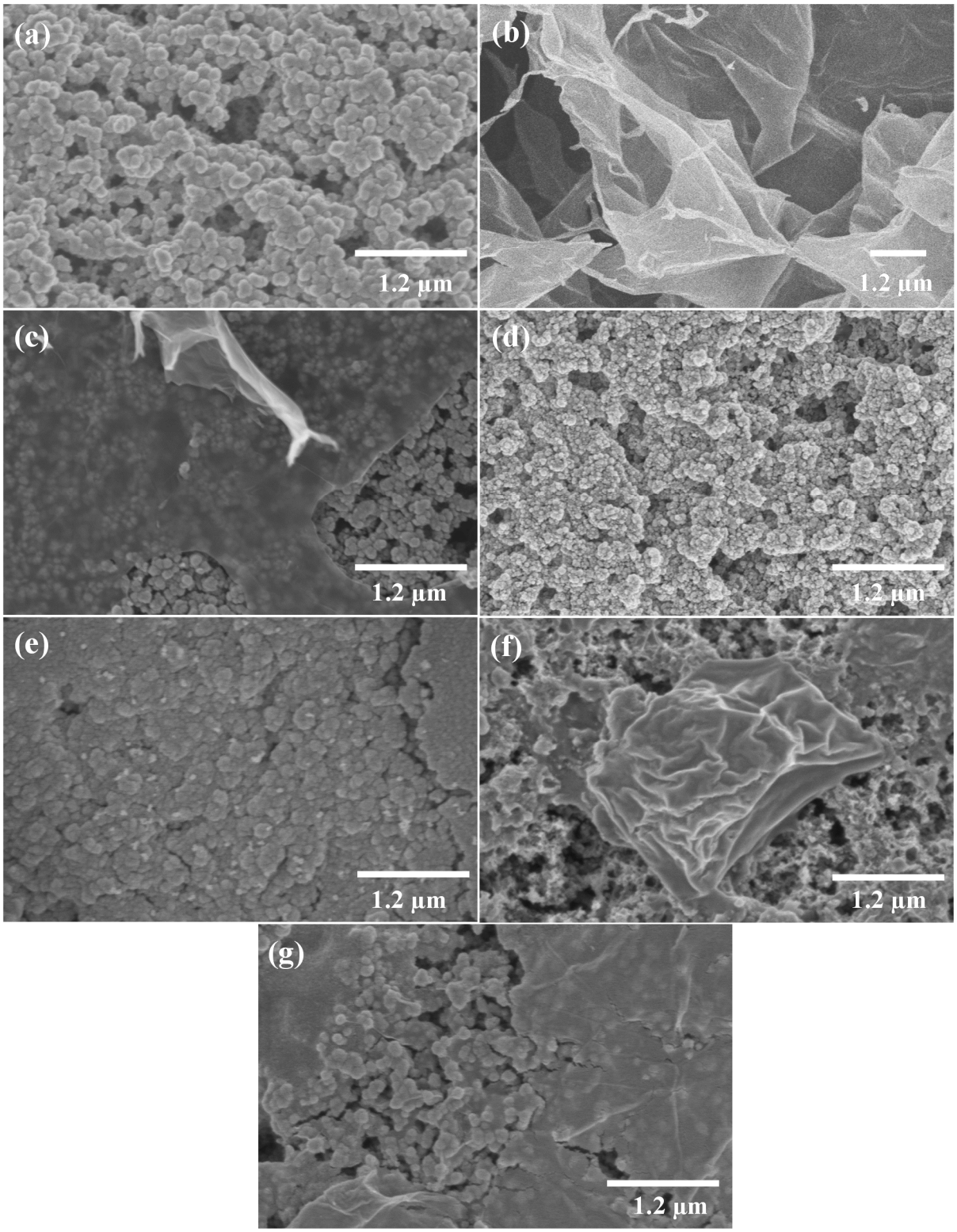

Fig. 4: SEM images of prepared T (a), G (b), GT (c), N (d), NT (e), NG (f) and NGT (g) samples.

Both HER and OER activity of the designed samples was evaluated by the linear voltammetry (LV) curves in an acidic medium of H_2SO_4 at a scan rate of 5 mV/s with current density normalized by surface area [72]. As shown in Fig. 5a and 5b, both T and G samples exhibit negligible HER and OER activity, whereas hybrid between Ni/TiO_2 or rGO/Ni could significantly enhance the HER and OER performance due to the generation of more active sites [73, 74]. As displayed in Fig 5b, to achieve a 10 mA/cm^{-2} HER current density in 0.5 M H_2SO_4 solution overpotentials of 430, 409, 314, 244, 130 mV for GT, N, NT, NG and NGT samples, respectively, is required. The durability of NGT sample was assessed through the chronoamperometric test at onset potential for both HER and OER electrolysis over 60 h. As revealed in Fig 5d, the current – time (i-t) chronoamperometric response exhibits a very slow attenuation with high current retention (97%) after 60 h. The XRD pattern of the prepared NGT sample after 60 hours of electrolysis test (Fig. S3) reveals that the structure remains unaltered. These results confirm that the catalyst possesses superior efficiency and stability in the long term HER and OER electrocatalysts compared to previously reported systems (Table S3). The better activity and durability of NGT electrode can be ascribed to the unique confined structure of both Ni/NiO and TiO_2 within graphene layers, which can enhance their interfacial contact, suppress the dissolution/agglomeration, and facilitate the transport of electrolyte ions [73, 74]. At the same time, NGT shows the optimally high electrocatalytic HER and OER activity among all the samples, where the production of hydrogen requires high current densities. Hydrogen atoms, formed upon H_2O discharge on both Ni/NiO and TiO_2 spill onto the rGO layers on the surface, which serves as an acceptor for H_{ads} atoms, enabling continuous cleaning of active sites and an alternative pathway for H_2 production. This mode of action is rendered by the unique reactivity of Ni/NiO, which arises due to the presence of Ni species connected on the surface of rGO structure.

Kinetics of HER were studied via Tafel equation in the form of ($\eta = b \log j + \alpha$), where j is the current density and η stands for the electrode overpotential, α and b are the Tafel intercept and the Tafel slope, respectively, the latter being an intensive quantity [75, 76]. Thus, Tafel slope only depends on the reaction mechanism and not on the size of the electrode. For this reason, b is an important parameter, which determines the reaction mechanism or its rate-determining step because the Tafel slope has defined values for a number of known electrode reactions and reaction

mechanisms. From the extrapolation of the linear plots of overpotential (η) vs log j as illustrated in Fig. 5e and Table 1, the Tafel slopes of 250, 210, 126, 120, 112, 54 and 40 mV/dec (after iR correction) are acquired by T, G, GT, N, NT, NG and NGT samples, respectively. According to the classic theory, the HER in acidic aqueous media proceeds in two steps as interpreted in the following equations:

The first step is an electrochemical reduction ($H_3O^+ + e^- \rightarrow H_{ads} + H_2O$) via discharge or Volmer step with Tafel slope ~120 mV/dec. *The second step* is the desorption of H_{ads} via two different pathways. One way is Heyrovsky reaction ($H_{ads} + H_3O^+ + e^- \rightarrow H_2 + H_2O$) via ion and atom reaction with slope ~ 40 mv/dec as presented in Fig. 6. The other possibility is Tafel reaction ($H_{ads} + H_{ads} \rightarrow H_2$) via atoms combination reaction with a slope of ~30 mV/dec. Consequently, the prepared electrodes have traced Volmer- Heyrovsky pathway as presented in Fig. 7.

The combination of rGO, Ni, and NiO/TiO_2 (*p-n* junction) in one heterostructure is very effective concept in improving the bifunctional catalytic performance of Ni/NiO/TiO_2/rGO@CC electrode for both HER and OER as overall water splitting reaction. As depicted in Fig. 7, within the *p-n* junction, the electrons flow from *n*-type TiO_2 to *p*-type NiO while the holes diffuse from the NiO to TiO_2, leading to a shift in the energy levels of both materials. Thus, under charge equilibrium, the *p*-type NiO region becomes rich with negative electron charges, while the positive hole charges are accumulated in the *n*-type TiO_2 region. The resulted negative charges can act as active centers at the surface of *p*-type NiO, facilitating the adsorption and reduction of protons (H^+) in acidic electrolyte. In the meantime, the positive charges accumulated in the *n*-type TiO_2 accelerate the transfer of electrons derived from H_2O oxidation during OER process. In order to maintain the charge balance inside the electrocatalyst, the redundant electrons and holes after HER and OER processes can be recombined together or compensated through applying enough potential via the external circuit. Moreover, the metallic Ni and rGO could enhance the charge transfer within the electrocatalyst. Thus, Ni/NiO/TiO_2/rGO@CC can be an efficient electrocatalyst for both OER and HER. The evidently reduced slope of NGT, compared with other samples, confirms the promoted Volmer step in HER kinetics. The small Tafel slope of NGT indicates a fast increase of the hydrogen generation rate with the applied overpotential, corresponding to the high activity presented in the LV curves.

To further access information about the active sites, the electrical double-layer capacitance (C_{dl}) is calculated as shown in Fig. 5f and listed in table 1. However, the electrochemical active surface area (EASA) of NGT sample is estimated to be around 525 cm^2, suggesting easy access to charge between electrode and electrolyte, and hence a maximum activity can be achieved.

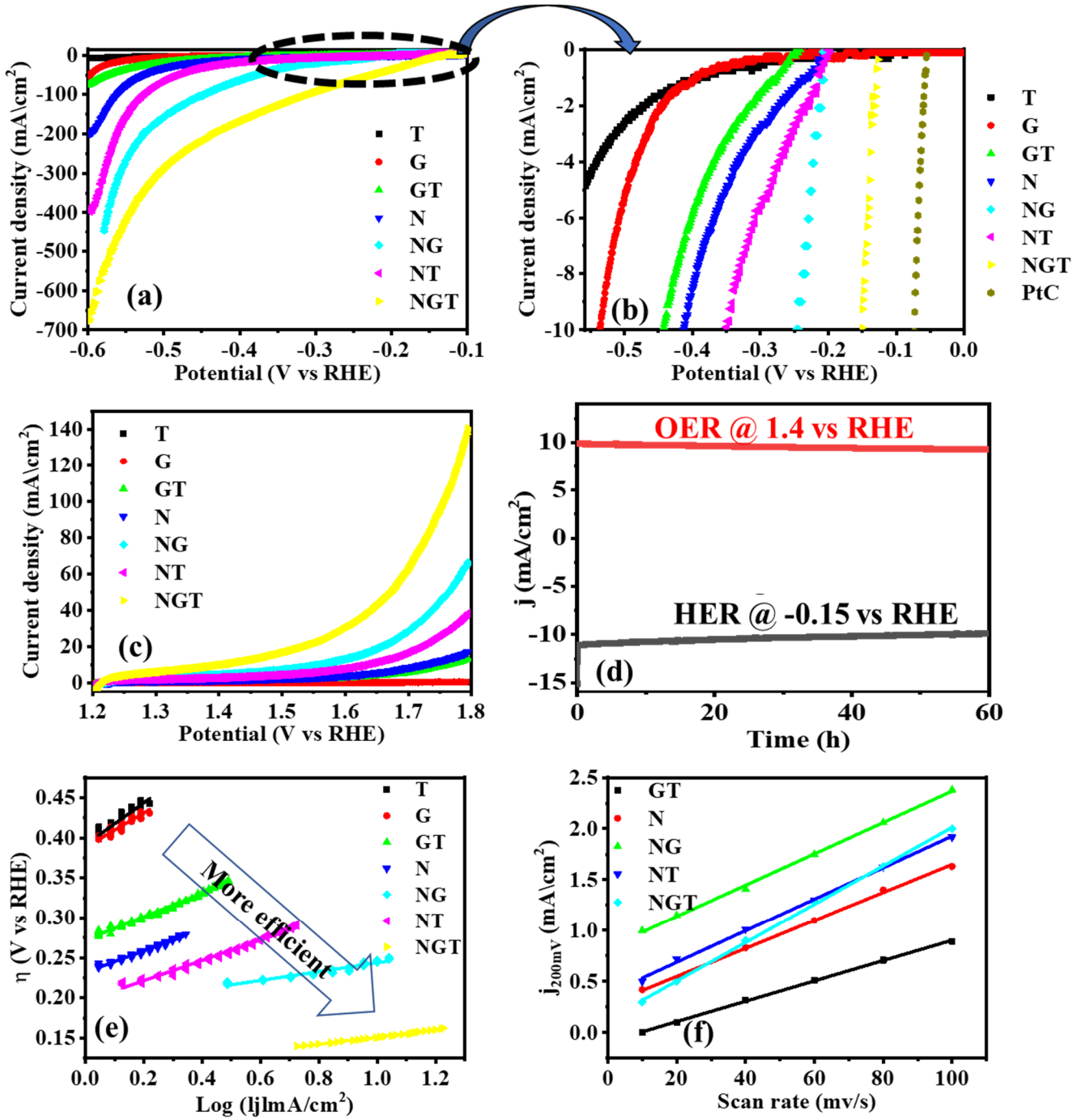

Fig. 5. (a, b) LV curves for HER, (c) LV curves for OER, (d) chronoamperometry test for NGT, (e) Tofel plots for HER and (f) estimation of C_{dl} through plotting the

current density variation ($\Delta j=(j_a-j_c)/2$, at 200 mv vs RHE; data obtained from the CV in Fig.S4) against scan rate to fit a linear regression.

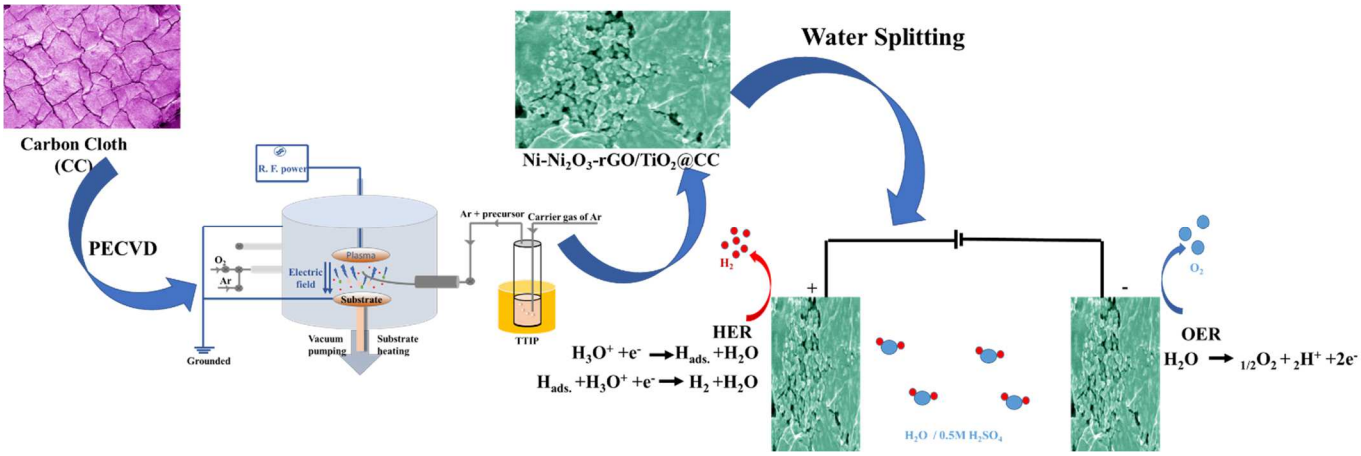

Fig. 6. Schematic diagram of synthesis and efficiency for Ni/NiOTiO$_2$/rGO@CC

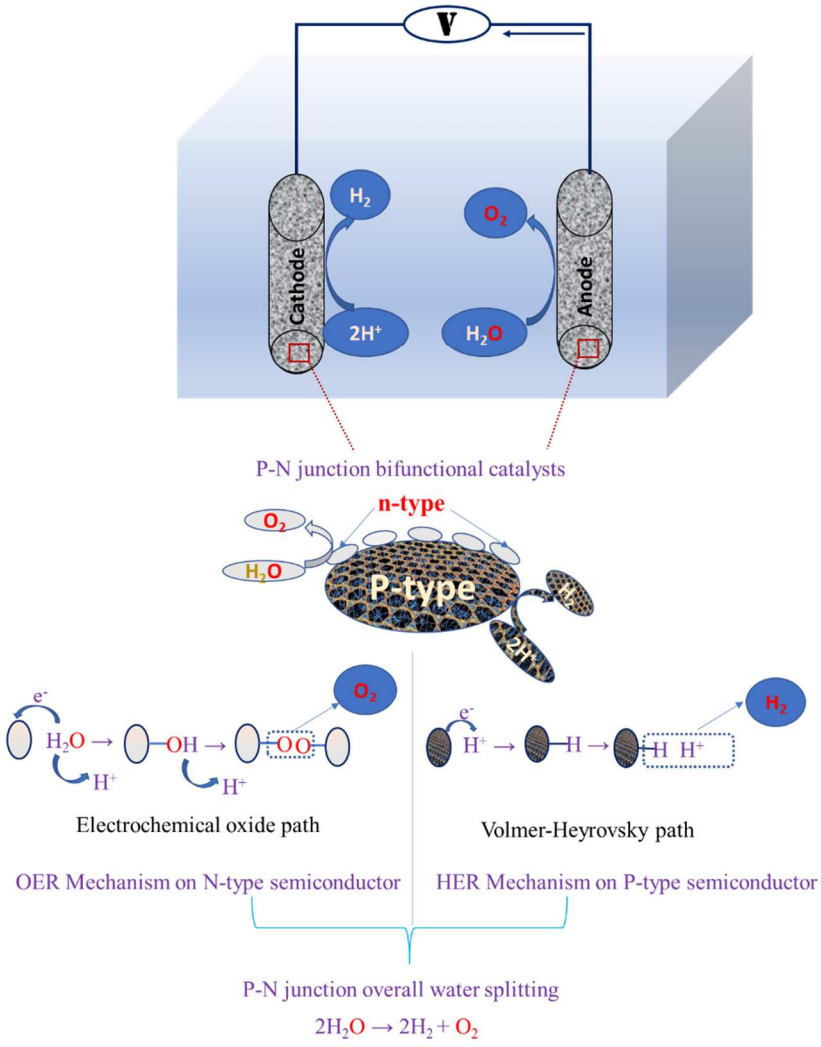

Fig. 7. schematic diagram explains the mechanism of improving the catalytic performance of PN junction within water splitting over Ni/NiOTiO$_2$/rGO@CC

Table 1. Electrochemical data of various prepared samples for HER and OER in 0.5 M H_2SO_4.

Samples	$\eta_{10(HER)}$ (mv)	TS_{HER} (mv/dec)	C_{dl} (mF/cm^2)	EASA (cm^2)	$\eta_{onset\ (OER)}$ (mv)	j_0 (A/cm^2)	R_s (Ω)	R_{ct} (Ω)
T	610	250	--	--	490	0.067	2	189
G	500	210	--	--	450	0.080	1.9	160
GT	430	126	9	225	370	0.088	2.3	145
N	409	120	13	325	260	1.42	3.4	9
NT	330	112	15	375	180	1.52	3.6	8.4
NG	244	54	16	400	90	2.13	3.7	6
NGT	130	40	21	525	30	4.28	4	3

η_{10}: Overpotential at 10 mA/ cm^2, η_{onset}: Onset potential, TS: Tafel slope of HER,

The excellent HER and OER performance of prepared samples are originated from the fast charge transfer and transport process, as evidenced via the electrochemical impedance measurements in Fig. 7. Specifically, NGT sample exhibits the lowest intrinsic resistance as indicated by the steepest slope in the low-frequency region and smallest charge transfer resistance as it shows the smallest semicircle in the high-frequency region. As illustrated in Fig 7e, the data of the solution resistance R_s and charge transfer resistance R_{ct} are calculated using an equivalent circuit and listed in Table 1.

The exchange current density (j_0) of prepared samples are further calculated from EIS data, which is the most ingrained measure of HER activity. As listed in Table 1, the j_0 of 4.28 A/cm^2 is calculated for NGT, which is higher than that of the other samples.

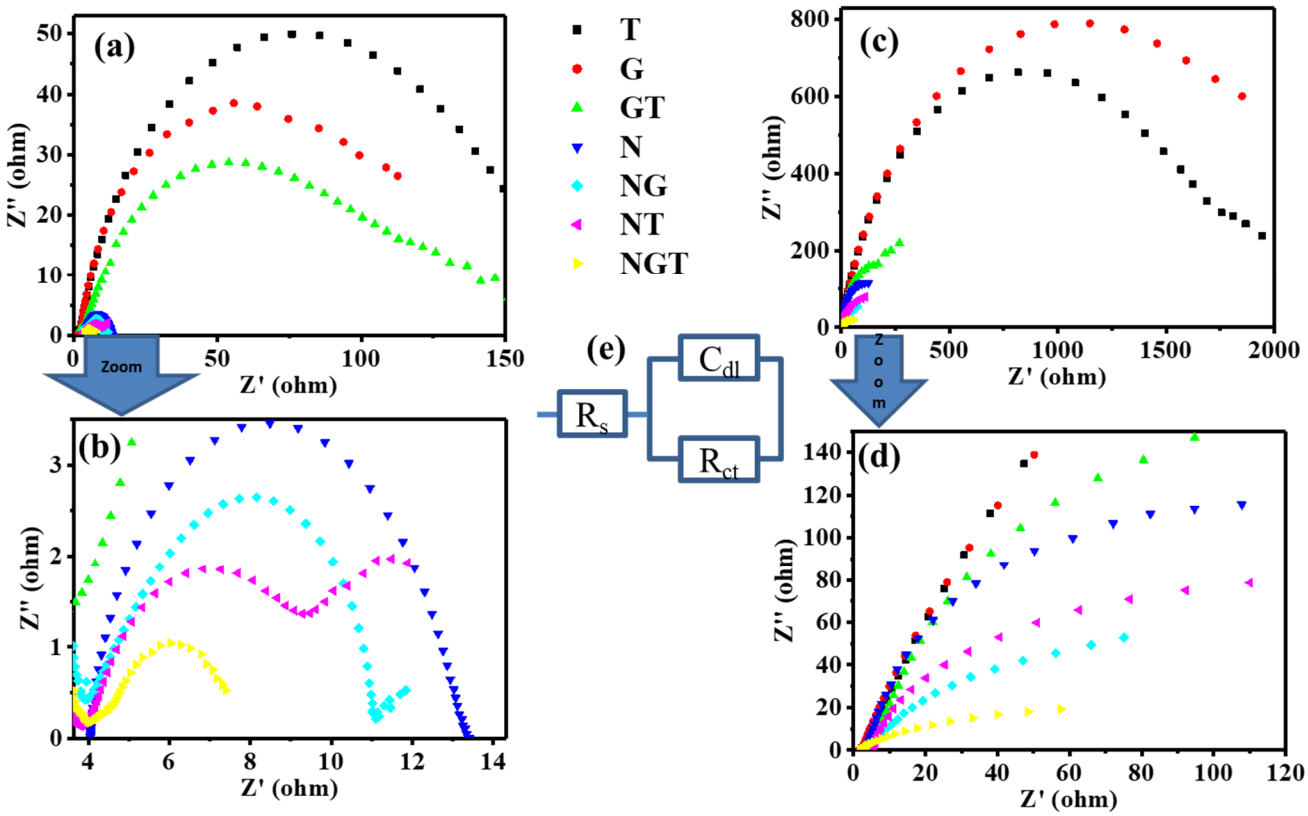

Fig. 7: EIS Nyquist plots in the frequency range of 0.1 Hz to 1M Hz obtained for (a,b) HER at -0.2 V vs RHE, (c,d) OER at 1.4 V vs RHE and (e) the proposed equivalent circuit.

Conclusion

Herein, we present a facile one-step approach for constructing a three-dimensional bifunctional electrocatalyst for water splitting application. Thus, a Ni/NiO/TiO_2/rGO electrocatalyst, prepared by the PECVD method, exhibits outstanding electrocatalytic activity with a low cell voltage of 130 mV to drive current density of 10 mA/cm^2. Furthermore, it shows superior durability, maintaining its high catalytic activity for at least 60 h in acidic media. The surface appearance, composition, and the phase structure of all prepared materials are analyzed using scanning electron microscopy (SEM), energy-dispersive X-ray spectroscopy (EDX), Raman and X-ray diffraction (XRD), respectively. XRD and Raman results confirm the coexistence of crystalline cubic NiO and anatase TiO_2 phases with particle size ranging from 5 to 30 nm. The results of XPS characterization reveal the partial reduction of NiO into metallic Ni^0 on the surface of NGT electrocatalyst. The outstanding electrocatalytic

activity of Ni/NiO/TiO_2/rGO electrocatalyst toward HER and OER can be contributed to the variation in surface morphology and the high number of active sites arising from the interactions between TiO_2 and Ni/NiO nanohybrids within graphene sheets. This work will open up new opportunities to develop high-performance and inexpensive electrocatalysts having great potential for renewable energy conversion systems via rational engineering of nanostructures and interfaces.

Acknowledgments

Amr A. Nada would like to acknowledge the support from the French Embassy in Egypt (Institut Français d'Egypte) and Academy of Scientific Research & Technology (ASRT) in the frame of IMHOTEP 2018-2019.

References

[1] Nada AA, Bekheet MF, Viter R, Miele P, Roualdes S, Bechelany M. BN/$Gd_xTi_{(1-x)}O_{(4-x)/2}$ nanofibers for enhanced photocatalytic hydrogen production under visible light. Applied Catalysis B: Environmental. 2019;251:76-86.

[2] Nada AA, El Rouby WMA, Bekheet MF, Antuch M, Weber M, Miele P, et al. Highly textured boron/nitrogen co-doped TiO_2 with honeycomb structure showing enhanced visible-light photoelectrocatalytic activity. Applied Surface Science. 2020;505.

[3] Hojamberdiev M, Bekheet MF, Hart JN, Vequizo JJM, Yamakata A, Yubuta K, et al. Elucidating the impact of A-site cation change on photocatalytic H_2 and O_2 evolution activities of perovskite-type $LnTaON_2$ (Ln = la and Pr). Physical Chemistry Chemical Physics. 2017;19:22210-20.

[4] Hojamberdiev M, Bekheet MF, Zahedi E, Wagata H, Kamei Y, Yubuta K, et al. New Dion-Jacobson Phase Three-Layer Perovskite $CsBa_2Ta_3O_{10}$ and Its Conversion to Nitrided $Ba_2Ta_3O_{10}$ Nanosheets via a Nitridation-Protonation-Intercalation-Exfoliation Route for Water Splitting. Crystal Growth and Design. 2016;16:2302-8.

[5] Kawrani S, Nada AA, Bekheet MF, Boulos M, Viter R, Roualdes S, et al. Enhancement of calcium copper titanium oxide photoelectrochemical performance using boron nitride nanosheets. Chemical Engineering Journal. 2020;389:124326.

[6] Hojamberdiev M, Bekheet MF, Zahedi E, Wagata H, Vequizo JJM, Yamakata A, et al. The contrasting effect of the Ta/Nb ratio in (111)-layered B-site deficient hexagonal perovskite $Ba_5Nb_{4-x}Ta_xO_{15}$ crystals on visible-light-induced photocatalytic water oxidation activity of their oxynitride derivatives. Dalton Transactions. 2016;45:12559-68.

[7] Ouyang C, Wang X, Wang C, Zhang X, Wu J, Ma Z, et al. Hierarchically porous Ni_3S_2 nanorod array foam as highly efficient electrocatalyst for hydrogen evolution reaction and oxygen evolution reaction. Electrochimica Acta. 2015;174:297-301.

[8] Cherevko S, Geiger S, Kasian O, Kulyk N, Grote J-P, Savan A, et al. Oxygen and hydrogen evolution reactions on Ru, RuO_2, Ir, and IrO_2 thin film electrodes in acidic and alkaline electrolytes: A comparative study on activity and stability. Catalysis Today. 2016;262:170-80.

[9] Jin H, Wang J, Su D, Wei Z, Pang Z, Wang Y. In situ cobalt–cobalt oxide/N-doped carbon hybrids as superior bifunctional electrocatalysts for hydrogen and oxygen evolution. Journal of the American Chemical Society. 2015;137:2688-94.
[10] Hu C, Dai L. Multifunctional carbon-based metal-free electrocatalysts for simultaneous oxygen reduction, oxygen evolution, and hydrogen evolution. Advanced Materials. 2017;29:1604942.
[11] Zhuang L, Ge L, Yang Y, Li M, Jia Y, Yao X, et al. Ultrathin Iron-Cobalt Oxide Nanosheets with Abundant Oxygen Vacancies for the Oxygen Evolution Reaction. Advanced Materials. 2017;29:1606793.
[12] Xu L, Jiang Q, Xiao Z, Li X, Huo J, Wang S, et al. Plasma-engraved Co_3O_4 nanosheets with oxygen vacancies and high surface area for the oxygen evolution reaction. Angewandte Chemie International Edition. 2016;55:5277-81.
[13] Han L, Yu XY, Lou XW. Formation of Prussian-Blue-Analog Nanocages via a Direct Etching Method and their Conversion into Ni–Co-Mixed Oxide for Enhanced Oxygen Evolution. Advanced materials. 2016;28:4601-5.
[14] Peng Z, Jia D, Al-Enizi AM, Elzatahry AA, Zheng G. From water oxidation to reduction: homologous Ni–Co based nanowires as complementary water splitting electrocatalysts. Advanced Energy Materials. 2015;5:1402031.
[15] Kellenberger A, Vaszilcsin N, Brandl W, Duteanu N. Kinetics of hydrogen evolution reaction on skeleton nickel and nickel–titanium electrodes obtained by thermal arc spraying technique. International Journal of Hydrogen Energy. 2007;32:3258-65.
[16] Digraskar RV, Mali SM, Tayade SB, Ghule AV, Sathe BR. Overall noble metal free Ni and Fe doped Cu_2ZnSnS_4 (CZTS) bifunctional electrocatalytic systems for enhanced water splitting reactions. International Journal of Hydrogen Energy. 2019;44:8144-55.
[17] Gao J, Jiang B, Ni C, Qi Y, Zhang Y, Oturan N, et al. Non-precious Co_3O_4-TiO_2/Ti cathode based electrocatalytic nitrate reduction: Preparation, performance and mechanism. Applied Catalysis B: Environmental. 2019;254:391-402.
[18] Browne MP, Sofer Z, Pumera M. Layered and two dimensional metal oxides for electrochemical energy conversion. Energy & Environmental Science. 2019;12:41-58.
[19] Zhang K, Huo Q, Zhou Y-Y, Wang H-H, Li G-P, Wang Y-W, et al. Textiles/Metal–Organic Frameworks Composites as Flexible Air Filters for Efficient Particulate Matter Removal. ACS Applied Materials & Interfaces. 2019;11:17368-74.
[20] Raj S, Anantharaj S, Kundu S, Roy P. In-situ Mn-Doping Promoted Conversion of $Co(OH)_2$ to Co_3O_4 as Active Electrocatalyst for Oxygen Evolution Reaction. ACS Sustainable Chemistry & Engineering. 2019;7:9690–8.
[21] Wu F, Wang C, Hu H-Y, Pan M, Li H-F, Xie N, et al. One-step synthesis of hierarchical metal oxide nanosheet/carbon nanotube composites by chemical vapor deposition. Journal of materials science. 2019;54:1291-303.
[22] Young C, Wang J, Kim J, Sugahara Y, Henzie J, Yamauchi Y. Controlled chemical vapor deposition for synthesis of nanowire arrays of metal–organic frameworks and their thermal conversion to carbon/metal oxide hybrid materials. Chemistry of Materials. 2018;30:3379-86.
[23] Chen K, Shi L, Zhang Y, Liu Z. Scalable chemical-vapour-deposition growth of three-dimensional graphene materials towards energy-related applications. Chemical Society Reviews. 2018;47:3018-36.
[24] Morosanu CE. Thin films by chemical vapour deposition: Elsevier; 2016.
[25] Saha S, Chhetri S, Khanra P, Samanta P, Koo H, Murmu NC, et al. In-situ hydrothermal synthesis of MnO_2/NiO@ Ni hetero structure electrode for hydrogen evolution reaction and high energy asymmetric supercapacitor applications. Journal of Energy Storage. 2016;6:22-31.

[26] Kong Q, Feng W, Ma S, Sun F, Xie X, Sun C. Hydrothermal Synthesis of Nanoporous NiO Rods Self-Supported on Ni Foam as Efficient Electrocatalysts for Hydrogen Evolution Reaction. JOM. 2019;71:621-5.
[27] Qi X, Su G, Bo G, Cao L, Liu W. Synthesis of NiO and NiO/TiO_2 films with electrochromic and photocatalytic activities. Surface and Coatings Technology. 2015;272:79-85.
[28] Ou G, Fan P, Zhang H, Huang K, Yang C, Yu W, et al. Large-scale hierarchical oxide nanostructures for high-performance electrocatalytic water splitting. Nano Energy. 2017;35:207-14.
[29] Gong M, Zhou W, Tsai M-C, Zhou J, Guan M, Lin M-C, et al. Nanoscale nickel oxide/nickel heterostructures for active hydrogen evolution electrocatalysis. Nature communications. 2014;5:4695.
[30] Peng Y, Jiang K, Hill W, Lu Z, Yao H, Wang H. Large-Scale, Low-Cost, and High-Efficiency Water-Splitting System for Clean H_2 Generation. ACS applied materials & interfaces. 2019;11:3971-7.
[31] McCarty JG, Gusman M, Lowe D, Hildenbrand D, Lau K. Stability of supported metal and supported metal oxide combustion catalysts. Catalysis Today. 1999;47:5-17.
[32] Lu S, Lian J, Zhang F, Jiang W, Hu Q, Li D, et al. $Fe_{40}Co_{40}Se_{20}$ Glassy Films Supported on Carbon Fiber Paper as Electrocatalysts in the Oxygen Evolution Reaction. Journal of The Electrochemical Society. 2019;166:F620-F6.
[33] Shang M, Wang W, Yin W, Ren J, Sun S, Zhang L. General Strategy for a Large-Scale Fabric with Branched Nanofiber–Nanorod Hierarchical Heterostructure: Controllable Synthesis and Applications. Chemistry–A European Journal. 2010;16:11412-9.
[34] Balogun MS, Qiu W, Luo Y, Huang Y, Yang H, Li M, et al. Improving the Lithium-Storage Properties of Self-Grown Nickel Oxide: A Back-Up from TiO_2 Nanoparticles. ChemElectroChem. 2015;2:1243-8.
[35] Wang J, Fan H, Shen Y, Li C, Wang G. Large-scale template-free synthesis of nitrogen-doped 3D carbon frameworks as low-cost ultra-long-life anodes for lithium-ion batteries. Chemical Engineering Journal. 2019;357:376-83.
[36] Liu Y, Gao C, Li Q, Pang H. Nickel Oxide/Graphene Composites: Synthesis and Applications. Chemistry–A European Journal. 2019;25:2141-60.
[37] Cai W, Zhou M, Cao D, Yan X, Li Q, Lü S, et al. Ni-doped A-site-deficient $La_{0.7}Sr_{0.3}Cr_{0.5}Mn_{0.5}O_{3-\delta}$ perovskite as anode of direct carbon solid oxide fuel cells. International Journal of Hydrogen Energy. 2020;45:21873-80.
[38] Keerthana SP, Rani BJ, Ravi G, Yuvakkumar R, Hong SI, Velauthapillai D, et al. Ni doped Bi_2WO_6 for electrochemical OER activity. International Journal of Hydrogen Energy. 2020;45:18859-66.
[39] Ramadoss A, Kim SJ. Improved activity of a graphene–TiO_2 hybrid electrode in an electrochemical supercapacitor. Carbon. 2013;63:434-45.
[40] Yu J, Zhou W, Xiong T, Wang A, Chen S, Chu B. Enhanced electrocatalytic activity of Co@ N-doped carbon nanotubes by ultrasmall defect-rich TiO_2 nanoparticles for hydrogen evolution reaction. Nano Research. 2017;10:2599-609.
[41] Tavakkoli M, Holmberg N, Kronberg R, Jiang H, Sainio J, Kauppinen EI, et al. Electrochemical activation of single-walled carbon nanotubes with pseudo-atomic-scale platinum for the hydrogen evolution reaction. Acs Catalysis. 2017;7:3121-30.
[42] Zhang X, Yu X, Zhang L, Zhou F, Liang Y, Wang R. Molybdenum Phosphide/Carbon Nanotube Hybrids as pH-Universal Electrocatalysts for Hydrogen Evolution Reaction. Advanced Functional Materials. 2018;28:1706523.
[43] Salehabadi A, Salavati-Niasari M, Ghiyasiyan-Arani M. Self-assembly of hydrogen storage materials based multi-walled carbon nanotubes (MWCNTs) and $Dy_3Fe_5O_{12}$ (DFO) nanoparticles. Journal of Alloys and Compounds. 2018;745:789-97.

[44] Ma W, Ma R, Wang C, Liang J, Liu X, Zhou K, et al. A superlattice of alternately stacked Ni–Fe hydroxide nanosheets and graphene for efficient splitting of water. ACS nano. 2015;9:1977-84.
[45] Kumar BS, Gudla VC, Ambat R, Kalpathy SK, Anandhan S. Graphene nanoclusters embedded nickel cobaltite nanofibers as multifunctional electrocatalyst for glucose sensing and water-splitting applications. Ceramics International. 2019;45:25078-91.
[46] Navarro-Pardo F, Tong X, Selopal GS, Cloutier SG, Sun S, Tavares AC, et al. Graphene oxide/cobalt-based nanohybrid electrodes for robust hydrogen generation. Applied Catalysis B: Environmental. 2019;245:167-76.
[47] Nada AA, Bekheet MF, Roualdes S, Gurlo A, Ayral A. Functionalization of MCM-41 with titanium oxynitride deposited via PECVD for enhanced removal of methylene blue. Journal of Molecular Liquids. 2019;274:505-15.
[48] El-Maghrabi HH, Nada AA, Diab KR, Youssef AM, Hamdy A, Roualdes S, et al. Facile fabrication of $NiTiO_3$/graphene nanocomposites for photocatalytic hydrogen generation. Journal of Photochemistry and Photobiology A: Chemistry. 2018;365:86-93.
[49] Hou Y, Zuo F, Dagg A, Feng P. Visible light-driven α-Fe_2O_3 nanorod/graphene/$BiV_{1-x}Mo_xO_4$ core/shell heterojunction array for efficient photoelectrochemical water splitting. Nano letters. 2012;12:6464-73.
[50] Chen C-J, Liao C-H, Hsu K-C, Wu Y-T, Wu JC. P–N junction mechanism on improved NiO/TiO_2 photocatalyst. Catalysis communications. 2011;12:1307-10.
[51] Yu J, Hai Y, Cheng B. Enhanced Photocatalytic H_2-Production Activity of TiO_2 by $Ni(OH)_2$ Cluster Modification. The Journal of Physical Chemistry C. 2011;115:4953-8.
[52] Hu S, Li F, Fan Z, Gui J. Improved photocatalytic hydrogen production property over Ni/NiO/N–TiO_{2-x} heterojunction nanocomposite prepared by NH_3 plasma treatment. Journal of Power Sources. 2014;250:30-9.
[53] Zhang X, Chen N, Wang Y, Wu G, Du X. Self-supported multidimensional Ni–Fe phosphide networks as novel and robust water splitting catalyst. International Journal of Hydrogen Energy. 2020;45:22921-8.
[54] Zong H, Yu K, Zhu Z. Heterostructure nanohybrids of Ni-doped $MoSe_2$ coupled with Ti_2NT_x toward efficient overall water splitting. Electrochimica Acta. 2020;353:136598.
[55] Narwade SS, Mali SM, Digraskar RV, Sapner VS, Sathe BR. Ni/NiO@rGO as an efficient bifunctional electrocatalyst for enhanced overall water splitting reactions. International Journal of Hydrogen Energy. 2019;44:27001-9.
[56] Kawrani S, Boulos M, Bekheet MF, Viter R, Nada AA, Riedel W, et al. Segregation of copper oxide on calcium copper titanate surface induced by Graphene Oxide for Water splitting applications. Applied Surface Science. 2020;516:146051.
[57] Nada AA, Tantawy HR, Elsayed MA, Bechelany M, Elmowafy ME. Elaboration of nano titania-magnetic reduced graphene oxide for degradation of tartrazine dye in aqueous solution. Solid State Sciences. 2018;78:116-25.
[58] Yang Z, He R, Wu H, Ding Y, Mei H. Needle-like CoP/rGO growth on nickel foam as an efficient electrocatalyst for hydrogen evolution reaction. International Journal of Hydrogen Energy. 2020:In Press.
[59] Sudarsono W, Wong WY, Loh KS, Majlan EH, Syarif N, Kok K-Y, et al. Sengon wood-derived RGO supported Fe-based electrocatalyst with stabilized graphitic N-bond for oxygen reduction reaction in acidic medium. International Journal of Hydrogen Energy. 2020;45:23237-53.
[60] Ghasemi R, Moghadas BK, Mohammadi I. Solvothermal synthesis of Pd_{10}–Ni_{45}–Co_{45}/rGO composites as novel electrocatalysts for enhancement of the performance of DBFC. International Journal of Hydrogen Energy. 2020;45:21808-15.
[61] Youssef L, Roualdès S, Bassil J, Zakhour M, Rouessac V, Lamy C, et al. Effect of plasma power on the semiconducting behavior of low-frequency PECVD TiO_2 and nitrogen-doped TiO_2 anodic thin coatings: photo-electrochemical studies in a single compartment cell for

hydrogen generation by solar water splitting. Journal of Applied Electrochemistry. 2019;49:135-50.
[62] Shahriary L, Athawale AA. Graphene oxide synthesized by using modified hummers approach. Int J Renew Energy Environ Eng. 2014;2:58-63.
[63] El-Maghrabi HH, Abdelmaged SM, Nada AA, Zahran F, El-Wahab SA, Yahea D, et al. Magnetic graphene based nanocomposite for uranium scavenging. Journal of hazardous materials. 2017;322:370-9.
[64] El-Maghrabi HH, Nada EA, Soliman FS, Moustafa YM, Amin AE-S. One pot environmental friendly nanocomposite synthesis of novel TiO_2-nanotubes on graphene sheets as effective photocatalyst. Egyptian Journal of Petroleum. 2016;25:575-84.
[65] Nada AA, Nasr M, Viter R, Miele P, Roualdes Sp, Bechelany M. Mesoporous $ZnFe_2O_4$@TiO_2 nanofibers prepared by electrospinning coupled to PECVD as highly performing photocatalytic materials. The Journal of Physical Chemistry C. 2017;121:24669-77.
[66] Yu T, Liu H, Huang M, Zhang J, Su D, Tang Z, et al. Zn_2GeO_4 nanorods grown on carbon cloth as high performance flexible lithium-ion battery anodes. RSC Advances. 2017;7:51807-13.
[67] Liu W, Lu C, Wang X, Liang K, Tay BK. In situ fabrication of three-dimensional, ultrathin graphite/carbon nanotube/NiO composite as binder-free electrode for high-performance energy storage. Journal of Materials Chemistry A. 2015;3:624-33.
[68] Li C, Hou J, Wu Z, Guo K, Wang D, Zhai T, et al. Acid promoted Ni/NiO monolithic electrode for overall water splitting in alkaline medium. Science China Materials. 2017;60:918-28.
[69] Barhoum A, El-Maghrabi HH, Iatsunskyi I, Coy E, Renard A, Salameh C, et al. Atomic layer deposition of Pd nanoparticles on self-supported carbon-Ni/NiO-Pd nanofiber electrodes for electrochemical hydrogen and oxygen evolution reactions. Journal of colloid and interface science. 2020;569:286-97.
[70] Ohsaka T, Izumi F, Fujiki Y. Raman spectrum of anatase, TiO_2. Journal of Raman spectroscopy. 1978;7:321-4.
[71] Kordek K, Yin H, Rutkowski P, Zhao H. Cobalt-based composite films on electrochemically activated carbon cloth as high performance overall water splitting electrodes. International Journal of Hydrogen Energy. 2019;44:23-33.
[72] Jiao Y, Zheng Y, Jaroniec M, Qiao SZ. Design of electrocatalysts for oxygen-and hydrogen-involving energy conversion reactions. Chemical Society Reviews. 2015;44:2060-86.
[73] Kullaiah R, Elias L, Hegde AC. Effect of TiO_2 nanoparticles on hydrogen evolution reaction activity of Ni coatings. International Journal of Minerals, Metallurgy, and Materials. 2018;25:472-9.
[74] Chanda D, Hnát J, Dobrota AS, Pašti IA, Paidar M, Bouzek K. The effect of surface modification by reduced graphene oxide on the electrocatalytic activity of nickel towards the hydrogen evolution reaction. Physical Chemistry Chemical Physics. 2015;17:26864-74.
[75] Lasia A, Rami A. Kinetics of hydrogen evolution on nickel electrodes. Journal of electroanalytical chemistry and interfacial electrochemistry. 1990;294:123-41.
[76] Lasia A. Mechanism and kinetics of the hydrogen evolution reaction. International Journal of Hydrogen Energy. 2019;44:19484-518.

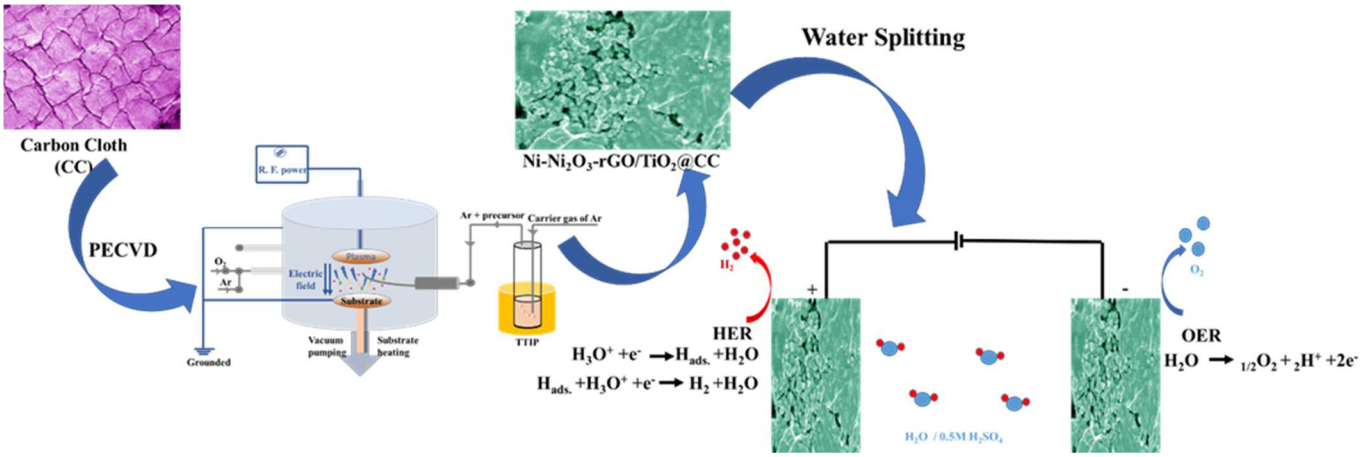
Carbon Cloth
(CC)
PECVD
R. F. power
O2
Ar
Electric field
Plasma
Substrate
Grounded
Vacuum pumping
Substrate heating
Ar + precursor
Carrier gas of Ar
TTIP
Ni-Ni2O3-rGO/TiO2@CC
Water Splitting
H2
HER
H3O+ +e- → Hads. +H2O
Hads. +H3O+ +e- → H2 +H2O
+
-
H2O / 0.5M H2SO4
O2
OER
H2O → 1/2O2 + 2H+ +2e-